Taylor & Francis
Taylor & Francis Group

Effect of Surface Morphology on Crack Growth at a Sol-Gel Reinforced Epoxy/Aluminum Interface

Jiong Liu
Manoj K. Chaudhury
Department of Chemical Engineering, Lehigh University,
Bethlehem, Pennsylvania, USA

Douglas H. Berry
Jill E. Seebergh
Joseph H. Osborne
Kay Y. Blohowiak
Boeing Company, Seattle, Washington, USA

The Boeing sol-gel conversion coating (Boegel-EPII), derived from an acid-catalyzed aqueous solution of organofunctional silane and zirconium alkoxide precursors, is being used as an adhesion promoter for adhesive bonding and painting applications in the aerospace industry. A unique advantage of the sol-gel process is that strong and durable bonds are produced without the hazardous chemical usage and rinse-water requirements of conventional anodizing or etching processes. In this study, a fracture mechanics method was used to investigate the adhesion properties of sol-gel-reinforced epoxy/aluminum joints. The Hugh Brown asymmetric double cantilever beam (ADCB) wedge test was employed, which allowed the measurements of the critical energy-release rate, subcritical crack-growth kinetics, and threshold energy-release rate on a single sample in a reasonably short period of time. These experiments were carried out with aluminum substrates on which the surface morphology was systematically varied by polishing, sanding, grit-blasting, and chemical etching. X-ray photoelectron spectroscopy (XPS) and scanning electron microscopy (SEM) were used to identify the locus of failure. The surface morphology of the substrates was characterized with SEM, optical profilometry, and spreading kinetics. The macrorough structures drive the crack to within a thin epoxy layer close to the polymer/metal interface, which enhances the initial strength of the sol-gel-reinforced interface. The microroughness of the substrate is, however, more effective than the

macroroughness in enhancing the durability. Lastly, an attempt has been made to correlate the energy-release rate with the fractal dimension for sol-gel-reinforced joints with macrorough substrates.

1. INTRODUCTION

Although adhesive bonding is increasingly finding applications in aerospace, automotive, and other industries, its use in key structural applications is rather limited. A major concern is that the mechanical performance of the adhesive joints involving inorganic substrates may deteriorate upon exposure to aggressive service environments [1–3]. To improve the initial adhesion strength and durability of the adhesive joints, surface preparation is critical.

In the aerospace industry, the strongest and most durable adhesive bonds to metallic substrates involve etching and anodizing processes [4]. The disadvantage of these processes stems from the fact that strong acids, bases, and other toxic materials, such as chromates, are used. Because of the growing demands from government and environmental agencies to eliminate such substances from materials and manufacturing processes, significant research and development efforts have been directed toward organofunctional silane approaches as potential surface-preparation methods [5–10].

More recently, a sol-gel process (Boegel) was developed at Boeing (The Boeing Company, Seattle, WA, USA) [11–14]. Although this process is similar to the currently used grit-blasting/silane process [10], it offers several advantages. For example, it is less dependent on processing conditions, eliminates the elevated-temperature drying step, and can eliminate the grit-blasting step in many applications [15]. In the Boegel process (Figure 1), thin films are produced onto metal substrates from dilute aqueous solutions of an organofunctional silane and zirconium alkoxide precursor, both of which are hydrolyzed to hydroxides and react with the hydroxyl groups on the metal surface *via* condensation. The organic functional groups of the silane are chosen such that they will react with the polymeric resin; for instance, the glycidoxyl functionality of the coupling agent will react with the amine groups of the epoxy resins. In between the metal and polymer, a hybrid organic/inorganic coating is formed through the self-condensation cross-linking process. The bonded system provides strong adhesion protection against aggressive environments.
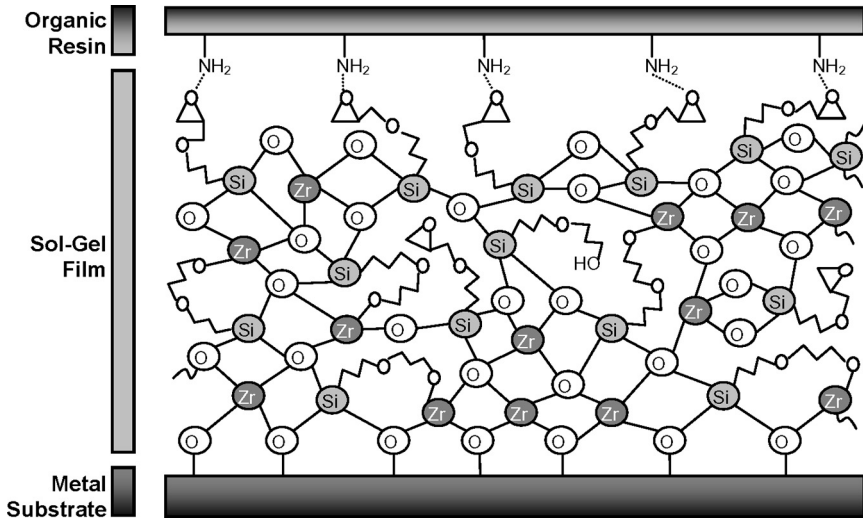
FIGURE 1 Schematic of a sol-gel adhesion promoting coating. The sol-gel film (typically 50–200 nm) is derived from the condensation reactions of a sol prepared from a mixture of glycidoxyl functional silane and zirconium alkoxide. An inorganic/organic gradient is created to achieve good adhesion. Variable-angle XPS studies indicate that the interface near the metal substrate is zirconia rich and the top film surface is silane rich [16].

Recent studies [11] have shown that the sol-gel process can produce adhesive joints with equivalent or superior strength and durability to the phosphoric acid anodizing (PAA) process, which is considered the "gold standard." Nevertheless, although the performance is promising, little is known about the precise adhesion-promoting mechanisms of the sol-gel-derived coatings. An issue of particular interest is how the surface pretreatment affects the adhesion strength and durability of the sol-gel-reinforced joints. Work done by Blohowiak *et al*. [13,15] and McCray *et al*. [17,18] demonstrated a large difference in hot/wet performance of the sol-gel coatings on substrates with a variety of pretreatment methods when assessed using the peel and DCB (double cantilever beam) wedge tests. Although valuable information has been obtained from these studies, the kinetics of the bond degradation upon exposure to hygrothermal and loading cycles is not completely understood.

The main objective of this study is to determine the effect of the surface pretreatment on adhesion strength and hydrolytic stability of the sol-gel-reinforced adhesive joint. For this purpose, a wedge test

employing an asymmetric double cantilever beam (ADCB) specimen was used to measure the crack-growth kinetics in humid environments along an epoxy/aluminum interface reinforced with sol-gel coating. The ADCB test was originally developed by Hugh Brown [19] and has been widely used [20–23] to measure the fracture energy of polymer/polymer interfaces. The advantage of the ADCB test is that with suitable design of the modulus and thickness of the two adherends, the crack can be forced to propagate close to the interface so that the effects of the surface pretreatment and sol-gel processing conditions can be directly evaluated. Our previous studies [24] demonstrated the applicability of the ADCB test method to investigate the toughness of the sol-gel-reinforced epoxy/aluminum interface. In the current study, the ADCB wedge test was slightly modified such that stable crack growth is ensured in a humid environment. X-ray photoelectron spectroscopy (XPS) and scanning electron microscopy (SEM) were used to identify the locus of failure. These studies were carried out with aluminum substrates for which the surface morphology was systematically varied by polishing, sanding, grit-blasting, and chemical etching. The surface roughness of the substrates was characterized with SEM, optical profilometry, and spreading kinetics. The correlation between the surface morphology and energy-release rate was examined.

2. EXPERIMENTAL

2.1. Materials

Clad 2024-T3 aluminum alloy (supplied by the Boeing Company, Seattle, WA, USA) was used as the substrate. The room temperature–curable epoxy system used in this study is based on diglycidyl ether of bisphenol-A (DGEBA) with an epoxide equivalent weight of 187.5 (EPON® 828, Resolution Performance Products, Houston, TX, USA). The curing agent is aminoethyl piperazine (EPICURE® 3200, Air Products and Chemicals, Inc., Allentown, PA, USA) (Figure 2). Five parts carboxylterminated butadiene acrylonitrile (Hycar® CTBN 1300X8, Noveon, Inc., Cleveland, OH, USA) per hundred parts DGEBA were used as toughener. CTBN was prereacted with the epoxy resin by mixing them at 140°C for 4 h to make an adduct. The resin adduct and curing agent were mixed thoroughly at the stoichiometric ratio, and the mixture was degassed by centrifugation. After applying onto the sol-gel-treated substrates, the resin was postcured according to the following protocol. The specimen was ramped from room temperature to 100°C in 4 h, held at 100°C for 2 h, and then cooled down

(a)

(b)
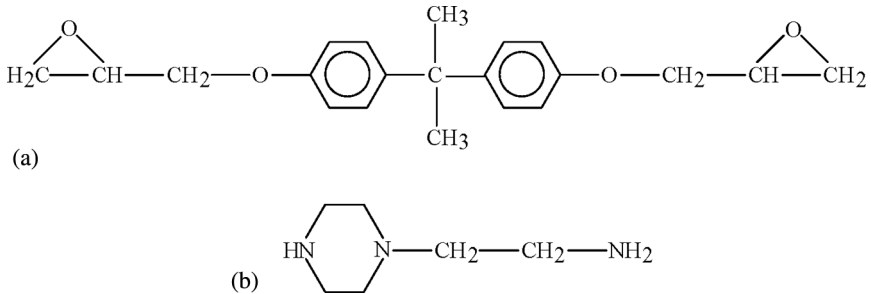
FIGURE 2 Chemical structure of the epoxy resin and curing agent: (a) diglycidyl ether of bisphenol-A (DGEBA); (b) aminoethyl piperazine (AEP).

to room temperature in 6 h. This cure procedure minimizes the residual thermal stress in the cured samples. The fracture behavior and toughening mechanisms for the bulk material of the present epoxy system were studied by Bagheri and Pearson [25,26]. The T_g of this epoxy as measured by differential scanning calorimetry was determined to be 105°C.

The sol-gel solutions were prepared following the procedures described in the literature for Boegel EPII [11–15]. Glycidoxypropyltrimethoxysilane (GPTMS, 97%, Gelest, Inc., Morrisville, PA, USA), zirconium tetrapropoxide (68–70%, Strem Chemicals, Inc., Newburyport, MA, USA), glacial acetic acid (Aldrich Chemical Co., Inc., St. Louis, MO, USA), and Antarox® BL-240 (Rhodia Inc., Cranbury, NJ, USA) were used as received. The resultant sol-gel solution was applied to the substrates within 2 h.

2.2. Surface Pretreatment

The as-received clad 2024-T3 aluminum alloy of thickness 1.6 mm was cut into 10 mm × 63.5 mm coupons. The substrates were wiped with methyl ethyl ketone and acetone, alkaline cleaned using Isoprep® 44 (MacDermid, Inc., Denver, CO, USA) solution at 60°C for 10 min, rinsed with water, and allowed to dry at room temperature. The samples were then subjected to various pretreatment methods, as summarized in Table 1, to create different surface morphologies on the substrates prior to the sol-gel application. Within 1 h after the pretreatment, the substrates were wetted by sol-gel solutions for 2 min, spun at 800 rpm for 50 s, and then allowed to dry at room temperature (25°C) and 47% ambient relative humidity (RH) for 75 min.

TABLE 1 Pretreatment Methods Used in the Present Study

Method	Description
Polishing	The substrates were ground mechanically with 600-grit silicon carbide paper, polished with 6 μm diamond paste, and cleaned with ethanol.
Chemical etching	The substrates were immersed in FPL (Forest Products Laboratory) solution [27] at 68°C for 10 min.
Sanding	The substrates were sanded with sandpaper of different grit sizes (Merit Abrasives, 120 grit, 180 grit, and 240 grit) using a random orbital sander. This particular type of sandpaper leads to a clean, uncontaminated surface as shown in previous Boeing studies [15].
Grit-blasting	The substrates were blasted with 50-μm alumina grit fluidized in 0.62 MPa pressurized air.
Grit-blasting and chemical etching combined[a]	Grit-blasting followed by chemical etching in FPL solution at 68°C for 10 min.

[a]The substrates treated by this method are denoted as "grit-blasted + FPL" in the text.

2.3. Specimen Preparation

The ADCB specimen (Figure 3) was prepared using the following procedure. After sol-gel application, a thin film of polytetrafluoroethylene (PTFE) was sprayed at the end of the substrate to serve as the precrack, after which the aluminum substrate was held in place at
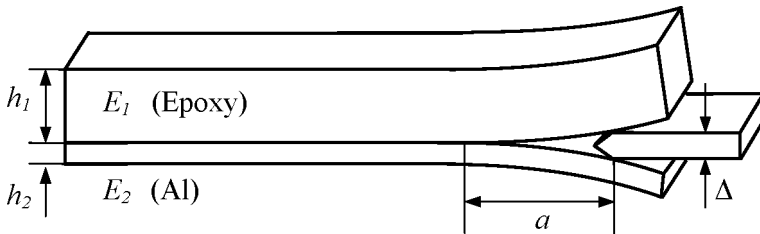
FIGURE 3 Schematic of the ADCB specimen. The strain energy-release rate for this specimen is a function of the crack length a, wedge thickness Δ, and materials constants E_1, E_2, h_1, and h_2, where E_1 and E_2 are the elastic moduli of epoxy and aluminum beams, respectively, and h_1 and h_2 stand for the thicknesses of the epoxy and aluminum beams, respectively.

the bottom of a silicone rubber mold, the width and length of which were exactly the same as those of the substrate. The uncured epoxy was then poured onto the substrate, and a glass slide bearing a thin PTFE film was placed on the top to squeeze out the extra epoxy. The thickness of the epoxy slab was controlled by the height of the mold. After the complete cure of the epoxy, the cover glass was detached and extra epoxy was cut off.

2.4. Crack-Growth Rate Measurement

The energy-release rate G for the ADCB specimen (Figure 3) is calculated using Kanninen's model of beams on elastic foundation [28], which has been validated by both boundary element and finite element analysis [29,30]. G is given by

$$G = \frac{3\Delta^2 E_1 h_1^3 E_2 h_2^3}{8a^4} \left[\frac{E_1 h_1^3 C_2^2 + E_2 h_2^3 C_1^2}{(E_1 h_1^3 C_2^3 + E_2 h_2^3 C_1^3)^2} \right], \tag{1}$$

where $C_1 = 1 + 0.64\, h_1/a$, $C_2 = 1 + 0.64\, h_2/a$, Δ is the wedge thickness, E is the elastic modulus, h is the beam thickness, a is the crack length, and subscripts 1 and 2 refer to epoxy beam and aluminum beam, respectively. Previous studies [20,24] have shown that the thickness ratio h_1/h_2 has a significant effect on the measured energy-release rate. The thickness ratio h_{Al}/h_{epoxy} in this study is held constant at ~ 0.25. This condition corresponds to a minimum energy-release rate, and the numerically estimated phase angle is $\sim 4°$ [24].

Figure 4 is a schematic of the ADCB wedge test setup. To study the hydrolytic stability of the epoxy/aluminum interfaces, the tests in this study were all carried out at 98% RH and $26 \pm 1°$C. The samples were conditioned in the environmental chamber for 1 h. No difference was found when a sample was conditioned for longer than 24 h. The details of the measurements are as follows: a razor blade with the thickness of 0.3 mm was inserted at the epoxy/aluminum interface to open the pre-crack, which was subsequently forced to propagate by pushing the blade at a constant speed of 7.6×10^{-5} m/s using an actuator controlled by a motor drive and a computer. A steady state was eventually reached, and the crack grew at about the same speed as the actuator. The fracture under this speed is denoted as the "high-velocity" region in the text. After the crack propagated about 3 mm at this speed, the motor was stopped. The growth of the crack over time was monitored and recorded using a microscope and a video camera. Monitoring lasted from 8 to 48 h and was stopped only when no additional crack growth was measured over a 5- to 6-h time period. A data series of
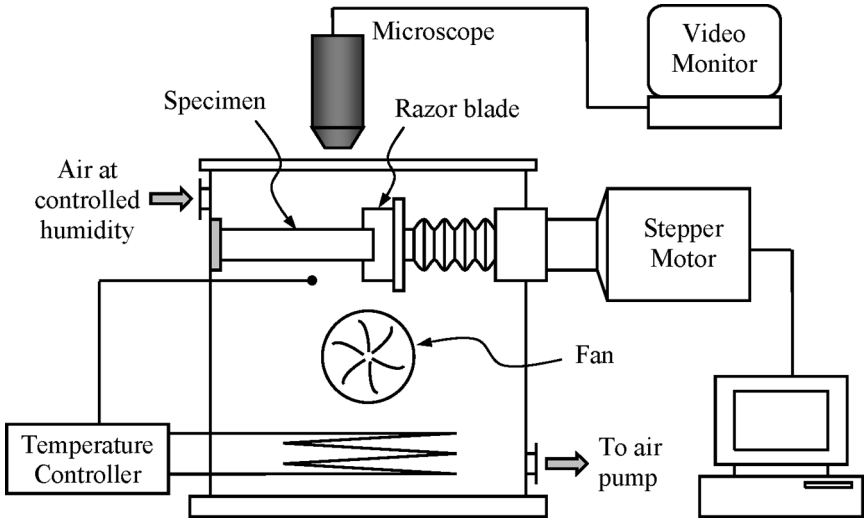
FIGURE 4 Schematic of the ADCB wedge-test setup. The specimen is fixed in an environmental chamber ($150 \times 140 \times 120$ mm) where the temperature and humidity are controlled. The measurements can be conducted in moist air as well as in water.

crack length as a function of time was obtained afterward and converted to crack growth velocity as a function of energy-release rate using the relationship given by Equation (1). After the test, the fracture surfaces were obtained by carefully applying an impact load from a thick wedge and a hammer. The fracture surfaces on both the aluminum and epoxy sides at the "high-velocity" and "crack-tip" regions were analyzed by XPS and SEM to identify the locus of failure. The "crack-tip" region represents the fracture surface produced at very low crack velocities, which is close to the crack tip when crack growth stops.

2.5. Characterization

A Stil Micromeasure optical profilometer (Micro Photonics, Irvine, CA, USA) was used to measure the surface roughness. The optical measuring pen had a measurement range of 350 µm, Z resolution of 10 nm, and lateral resolution of 1.8 µm. Five profile scans at different locations of the sample, each with a step size of 2.5 µm and full scale of 10 mm, were taken for each type of pretreatment. Figure 5 shows a typical profile of a grit-blasted sample. A 3D Mountains Map data postprocessing software [31] was used to obtain the roughness
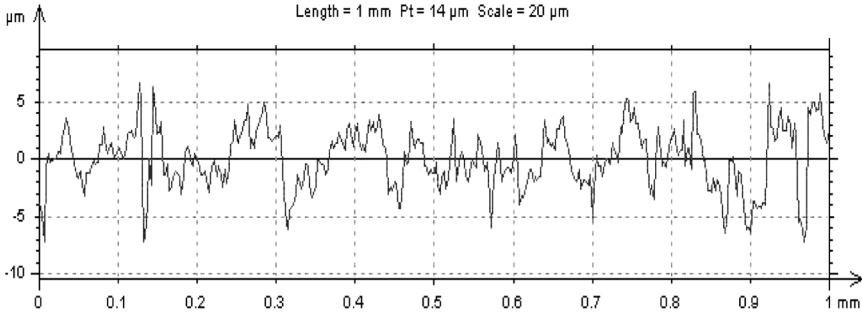
**FIGURE 5** Typical surface profile of a grit-blasted clad 2024-T3 substrate.

parameters and the fractal dimension from the profiles. The fractal dimension was evaluated using a box-counting method. This method consists of covering each part of a profile with a square of side length ε and counting the number, $N(\varepsilon)$, of all the squares in the whole profile. The same procedure is repeated for various ε values, and then $N(\varepsilon)$ is plotted versus $1/\varepsilon$ in a log-log plot. The slope, and hence the fractal dimension, D, is determined from

$$N(\varepsilon) = M \cdot \left(\frac{1}{\varepsilon}\right)^D, \tag{2}$$

where M is a constant related to the magnitude of the profile. Figure 6 shows typical log $(N(\varepsilon))-$log $(1/\varepsilon)$ plots for substrates with different pretreatments.

To validate the optical profilometry results, spreading kinetics experiments were carried out on substrates with various pretreatments. The procedure is as follows. A small drop $(2\,\mu l)$ of hexadecane (ReagentPlus[TM], 99%, Sigma-Aldrich, purified by passing it through neutral-grade alumina) was deposited onto the horizontally placed substrates at room temperature ($\sim 24°$C) and RH ($\sim 50\%$). The spreading process of the oil droplet as a function of time was monitored by a standard video camera and recorded with a VCR. Every experiment was repeated three times on separate samples for each pretreatment, and all the data are presented in Section 3.1.2.

The pretreated substrates before the sol-gel application, the sol-gel-treated substrates before bonding, and the fracture surfaces were examined using a JEOL (Tokyo, Japan) 6300 F scanning electron microscope with an Oxford (Bucks, UK) energy dispersive micro-analysis system and a Scienta (Gammadata, Uppsala, Sweden) ESCA-300 high-resolution X-ray photoelectron spectrometer. The
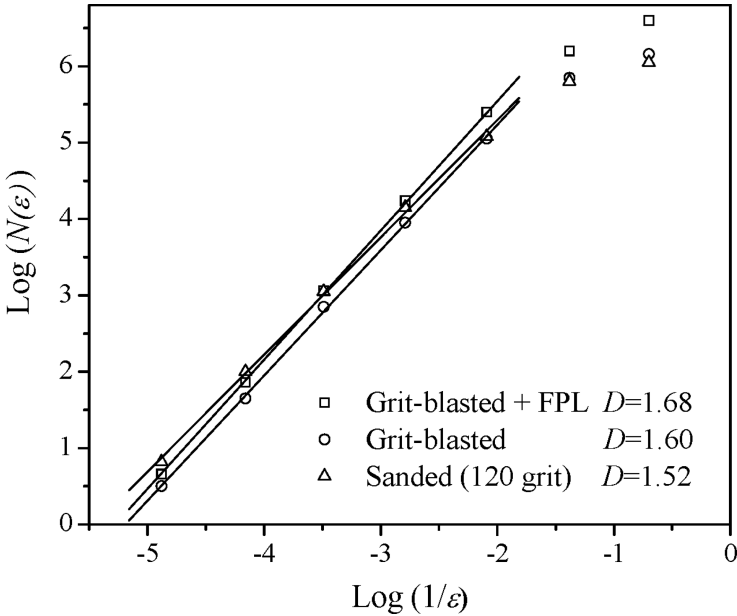
FIGURE 6 Typical $\log(N(\epsilon))$ *vs*. $\log(1/\epsilon)$ plots for substrates with different pretreatments. The fractal dimension D is given by the slope of the straight lines.

excitation radiation for the XPS was provided by a monochromatic Al $K\alpha$ X-ray source operated at a constant power of 4.5 kW and pass energy of 150 eV. The FWHM (Full width at half minimum) of the Ag 3d line was ~ 0.53 eV. The spot size was 3 mm $\times$ 0.5 mm. A flood gun was used to compensate the charging on the polymer samples. All spectra were taken at a 90° take-off angle. A survey scan was taken for each specimen to identify the elements on the surface, followed by a detailed high-resolution scan, to obtain the quantitative information for each element.

3. RESULTS AND DISCUSSION

3.1. Surface Morphology of the Pretreated Aluminum Substrates

3.1.1. Optical Profilometry and SEM

Surface pretreatment is a very important procedure before the sol-gel application in that it activates the alloy surface with a fresh oxide layer as well as provides appropriate surface morphology. Figure 7
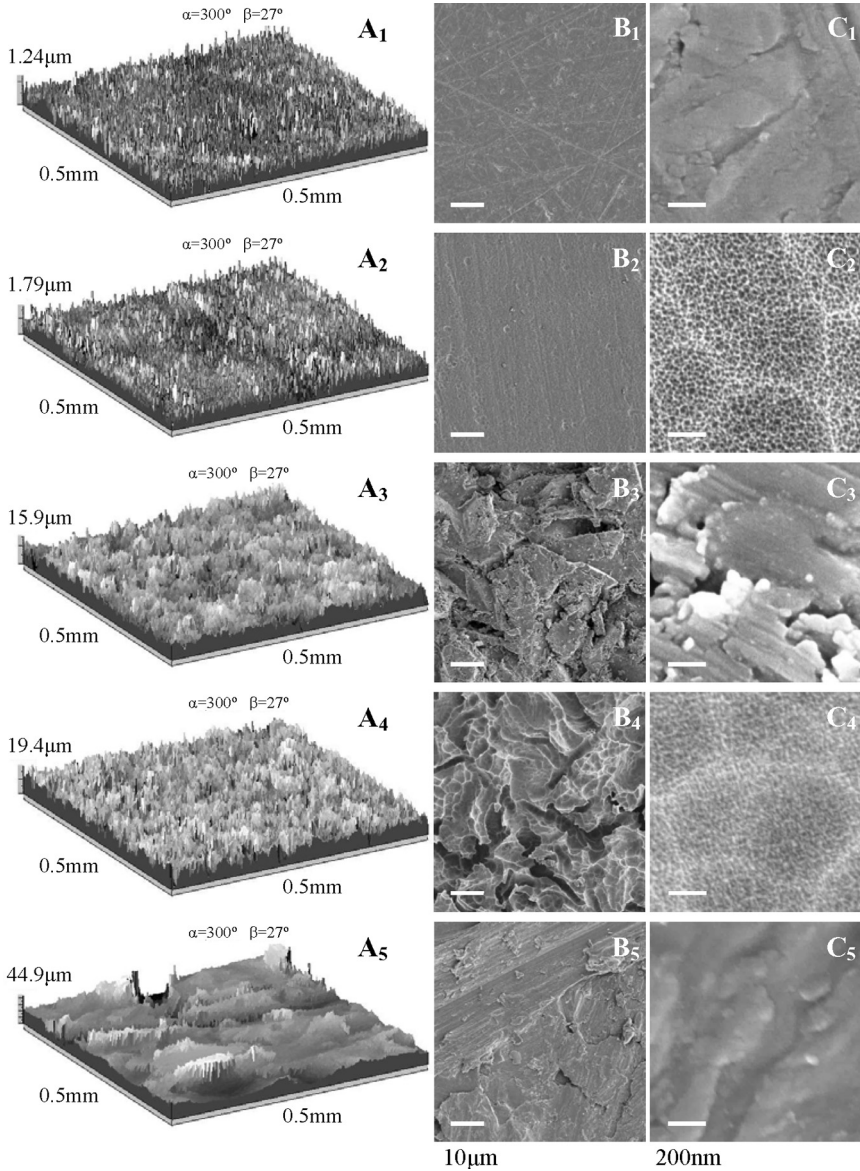
FIGURE 7 Surface morphology of clad 2024-T3 Al substrate with different pretreatment methods. A_1–A_5, 3D surface profiles obtained with optical profilometer; B_1–B_5, SEM photographs at $1000\times$; C_1–C_5, SEM photographs at $60,000\times$. Subscripts 1, 2, 3, 4, and 5 represent polished, FPL etched, grit-blasted, grit-blasted + FPL, and sanded (120 grit) substrates, respectively.

TABLE 2 Roughness Parameters and Fractal Dimension Measured with Optical Profilometry for Different Pretreatment Method

| Pretreatment | Roughness parameter[a] | | Fractal dimension D |
	R_a (μm)	R_t (μm)	
Polished	0.14 ± 0.004	1.50 ± 0.15	
FPL etched	0.19 ± 0.021	2.43 ± 0.29	
Grit-blasted	1.78 ± 0.07	17.28 ± 1.27	1.604 ± 0.027
Grit-blasted + FPL	2.74 ± 0.03	20.92 ± 0.87	1.672 ± 0.016
Sanded (120 grit)	2.30 ± 0.17	31.34 ± 4.70	1.518 ± 0.008
Sanded (180 grit)	1.75 ± 0.06	21.86 ± 1.27	1.538 ± 0.013
Sanded (240 grit)	1.51 ± 0.05	19.68 ± 2.06	1.532 ± 0.025

[a]R_a is the arithmetical mean deviation of the assessed profile. $R_a = (1/l) \int_0^l |y(x)| \, dx$, where l is the sampling length and y is the altitude of the profile. R_t is the total height of profile, which is the sum of the height of the largest profile peak height and the largest profile valley depth within the evaluation length [32].

shows the surface morphology of clad 2024-T3 aluminum substrate with different pretreatment methods. The 3D surface profiles obtained with profilometry and SEM photographs show that the dimensions of the roughness features are at different scales and the topography of the surfaces varies significantly with the pretreatment.

Table 2 gives a quantitative view of these surfaces. The listed two roughness parameters, average roughness, R_a, and peak-to-valley parameter, R_t, show similar trends as the pretreatment varies. Although the surface morphology differs drastically for the polished and FPL-etched substrates at the nanoscale (Figure 7C_1, C_2), at the micron scale the R_a and R_t values for these two substrates show only slight difference. Visually, both polished and FPL-etched substrates are macroscopically flat as compared with the grit-blasted and sanded substrates. Grit-blasting and sanding produce macrorough surfaces,[1] of which the R_a and R_t values are about one order of magnitude higher than that of the polished and FPL-etched substrates. Combining grit-blasting with FPL etching results in a surface with higher R_a, R_t values than those by grit-blasting only. For the sanded substrates, the macroroughness increases as the grit size of the sandpaper increases. Here the grit number is inversely proportional to the grit size.

[1]The most generally accepted definition of macroroughness and microroughness is given by Venables [27], where he defines macrorough surfaces as having characteristic bumps and jagged features about 1.0 μm or greater and microrough surfaces as having fine structure with dimensions 0.1 μm or less.

Although the roughness parameters R_a and R_t reveal the dimension of the roughness features on the surface, they give little information about the spatial distribution of the topography. The topography of most engineering surfaces is fractal in nature, exhibiting self-similar or self-affine scaling over a range of length scales [33,34]. Chemically etched surfaces have long been recognized as fractal at least over a range of dimensions smaller than the grain structure of the material [35]. Amada *et al*. [36–38] found that the grit-blasted surfaces have a self-affine property and evaluated their fractal dimension using a box-counting method. Mannelqvist and Groth [39] studied the surfaces created by several mechanical abrasion techniques and found that these surfaces show fractal behavior that can be characterized by fractal geometry.

In the present work, the fractal characteristics were investigated for the macrorough substrates based on the profile data obtained by the optical profilometer. The grit-blasted, sanded, and "grit-blasted + FPL" substrates all have fractal characteristics as confirmed by the linear relation between $\log(N(\varepsilon))$ and $\log(1/\varepsilon)$ values (Figure 6). Unlike R_a and R_t, the fractal dimensions of the sanded substrates are independent of grit size and are distinctly lower than that of the grit-blasted substrate. The "grit-blasted + FPL" substrate has the highest fractal dimension among all the substrates investigated.

It should be noted here that the fractal dimension of the polished and FPL-etched substrates could not be evaluated reliably with optical profilometry because of the limitations of the instrument. On the one hand, the optical profilometry only highlights the roughness features at the micron scale because of the limitation on lateral resolution. The microrough structures at the nanoscale were not captured by the instrument. Indeed, the surface morphologies of the polished and FPL-etched substrates were not distinguished by the optical profilometry (Figures 7A$_1$, 7A$_2$). Both substrates exhibit extremely random structures at the micron scale under the profilometer, even though the FPL-etched substrate is a well-known microrough surface that consists of a network of shallow pores and protrusions or whiskers [27] (Figure 7C$_2$, these structures can also be seen on the "grit-blasted + FPL" substrate in Figure 7C$_4$). On the other hand, the optical profilometer conducts an indirect altitude measurement, which consists in detecting the distance changes using an optical sensor. The sensitivity of the sensor depends on the roughness level of the substrate. As a consequence, an unreasonably high sensitivity was used for the polished and FPL-etched substrates because the micron-scale roughness features on these surfaces have dimensions comparable with the lateral resolution of the instrument ($1.8\,\mu m$). For this reason, the

fractal dimensions obtained for polished and FPL-etched surfaces are not comparable with those of the macrorough surfaces, on which the sensitivity used was much lower.

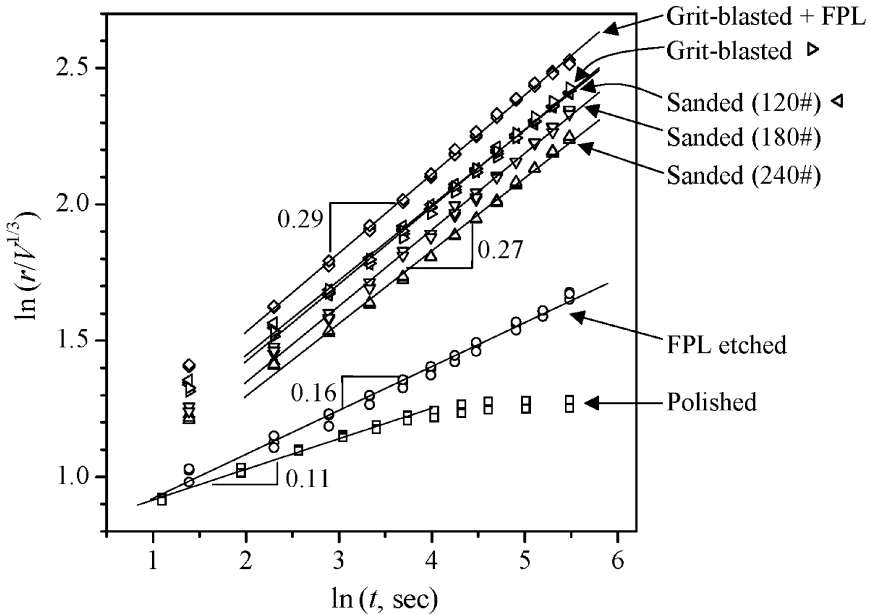### 3.1.2. Spreading Kinetics

   Spreading kinetics of a wetting liquid on a solid substrate may provide direct information about surface topography that would be useful for interpreting adhesion kinetics. Different kinetic regimes have already been identified in previous studies [40,48]. For example, a small liquid drop spreads on a perfectly smooth surface, in which the radius (r) of the drop increases with time (t) according to the following power law: $r \sim t^{0.1}$. As the roughness of the surface increases, the power law exponent increases. Thus, for a very rough surface, the power law may be expressed as $r \sim t^{0.25}$. For a fully rough surface where the spreading exponent of 0.25 is observed, the pre-exponential factor further increases with the ratio of the actual surface area to its
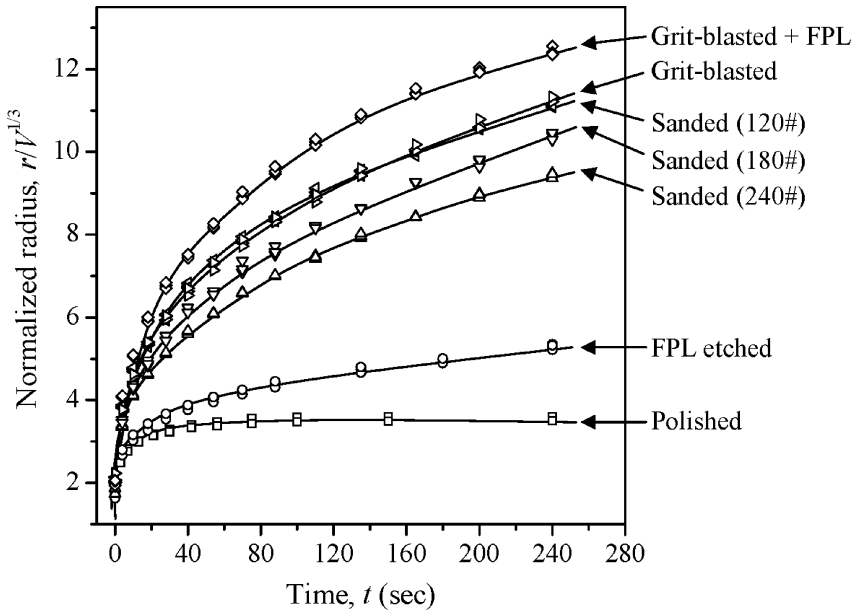
FIGURE 8 Spreading kinetics of a 2-μl hexadecane drop on clad 2024-T3 aluminum substrates with various pretreatments. The normalized radius of the drop is $r/V^{1/3}$, where V is the drop volume; 120#, 180#, and 240# represent sandpapers with different grit sizes.

geometric projection. Thus, from both the power law exponent and the pre-exponential factor, the surface roughness can be assessed.

Figure 8 summarizes the spreading kinetics results of a hexadecane drop on various pretreated substrates. It shows that hexadecane spreads much faster on the macrorough substrates (sanded, grit-blasted, and "grit-blasted + FPL") than on the polished and FPL-etched substrates. As the pretreatment changes, the trend of spreading velocity is qualitatively the same as that of average roughness, R_a, measured by profilometry. The logarithmic plots of spreading radius *vs.* time (Figure 9) show that the spreading exponent for hexadecane on the polished substrate is 0.11 during the active stage of spreading, which is similar to the values (0.1–0.14) reported in the literature [40–48] for liquids spreading on smooth surfaces. The spreading exponent of hexadecane on the FPL-etched substrate (0.16) is higher than on the smooth substrate. This result indicates that the microasperities on the FPL-etched substrate are able to reinitiate the spreading process; however, these initiation processes are not fully correlated as with the macrorough surfaces for which the limiting spreading exponents are observed.

FIGURE 9 Logarithmic plots of the spreading kinetics data of hexadecane on clad 2024-T3 aluminum substrates with various pretreatments; 120#, 180#, 240# represent sandpapers with different grit sizes.

For all the macrorough substrates (sanded, grit-blasted, and "grit-blasted + FPL"), the observed exponents during the active stage of spreading range from 0.27 to 0.29, which is close to 0.25 expected of macrorough surfaces [48]. Although the spreading exponents essentially do not change for different macrorough surfaces, the surface roughness is distinguished by the different intercepts of the logarithmic plot. For example, the intercept increases with the grit size of the sandpaper for the sanded substrates, which implies that the surface roughness increases with the grit size because a higher intercept means a higher ratio of the actual surface area to its geometric projection [48]. In addition, the "grit-blasted + FPL" surface shows the highest intercept, and thus the highest surface roughness, among all the pretreated surfaces. Those results agree with the optical profilometry measurements.

To summarize, the spreading kinetics results provide a supplementary view of the surface morphology of the substrates after various pretreatments. A fairly good correlation between the spreading kinetics and optical profilometry measurements further validates the surface profile data.

3.2. Crack Growth in Humid Environment

Figure 10 compares the moisture-assisted crack-growth velocity, V, plotted as a function of energy-release rate, G, for the sol-gel-treated epoxy/aluminum interfaces with different surface pretreatments. The measured crack-growth rate covers five orders of magnitude from 7.6×10^{-5} m/s to values approaching 10^{-9} m/s, with a concomitant decrease of the energy-release rate. This behavior is known as environmentally assisted or stress-corrosion cracking, which seems to involve the synergistic effects of an environment species, in this case moisture, and strained bonds at the crack tip [49].

The experimental data for different samples summarized in Figure 10 all exhibit a sigmoidal shape. They fit well with an equation that resembles the modified Paris law model [50,51]:

$$\frac{da}{dt} = CG^n \left[\frac{1 - (G_{th}/G)^{n_1}}{1 - (G/G_c)^{n_2}} \right], \tag{2}$$

where G_c is the critical energy-release rate; G_{th} is the threshold energy-release rate; and the empirical constants C, n, n_1, and n_2 are obtained by fitting the equation to the experimental data. Three regions are clearly seen. Region I corresponds to a lower bound that occurs at the threshold energy-release rate, G_{th}, where the crack-growth velocity is negligible. Region III corresponds to an upper
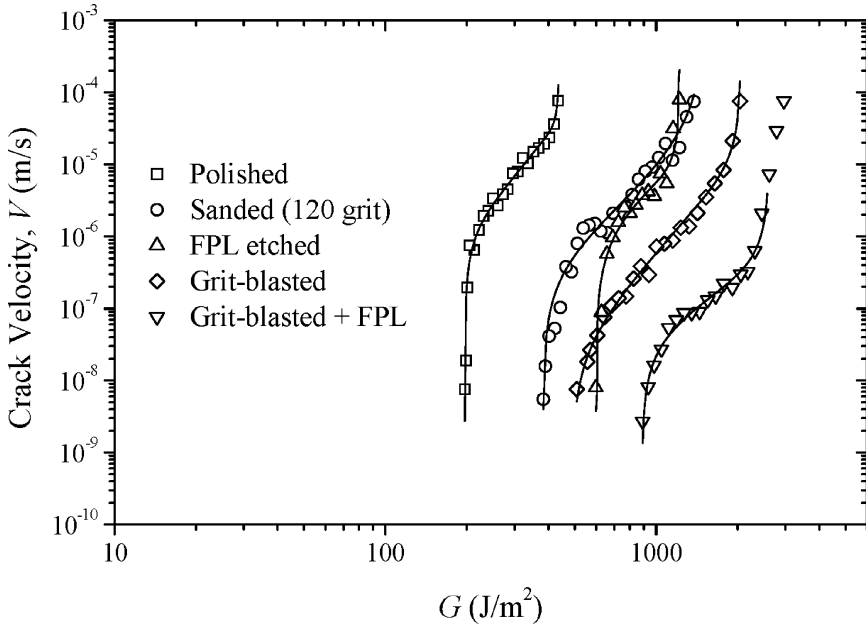
FIGURE 10 Crack growth velocity (26°C, 98% RH) as a function of energy-release rate for the sol-gel-treated aluminum/epoxy joints prepared with various surface pretreatments. The symbols represent the experimental data and the solid curves are the fitting results with a modified Paris law as given by Equation (2). Square: polished; circle: sanded with 120-grit sandpaper; diamond: grit-blasted; up triangle: FPL etched; down triangle: grit-blasted + FPL.

bound, G_c, which signifies the critical energy-release rate. Region II represents the linear region between regions I and III, where significant subcritical crack growth occurs. The exponent n is given by the slope of the linear region. Ritter [52] pointed out that n is a measure of the sensitivity of crack growth to the applied G; a higher n signifies a greater resistance to "stress-corrosion" crack growth. The curvature of the threshold "Region I" and the fast-fracture "Region III" are determined by n_1 and n_2 respectively.

The values of the parameters obtained from curve fitting using Equation (2) from Figure 10 are summarized in Table 3. An interesting observation for the sol-gel-treated epoxy/aluminum joints is that the trends on G_c and G_{th} are different as pretreatment changes. Among the four single pretreatments (polished, sanded, grit-blasted, and FPL etched), the grit-blasted substrate has the highest G_c, whereas the highest G_{th} is obtained on the FPL-etched substrate. A combination

TABLE 3 Values of the Parameters Obtained from Curve Fitting using Equation (2) based on Figure 10 Data

| Parameter	G_c J/m^2	G_{th} J/m^2	C m^2/N·s	n	n_1	n_2
Polished	440	196	2.1×10^{-17}	4.65	11.39	36.68
FPL etched	1225	598	1.5×10^{-14}	2.88	3.50	16.80
Sanded	1500	382	7.0×10^{-14}	2.00	3.00	0.02
Grit-blasted	2060	490	3.2×10^{-19}	4.10	3.55	9.28
Grit-blasted + FPL	2615	884	7.0×10^{-16}	2.60	5.50	8.04

of grit-blasting and FPL etching results in G_c and G_{th} values both significantly higher than all other pretreatments. The kinetics of the crack growth shows several intriguing features. In the linear region II, the value of the exponent n seems to be insensitive to pretreatment method. The coefficient C corresponding to the linear region II varies significantly as pretreatments changes, covering several orders of magnitude. In addition, the curve-fitting constant n_1 of region I appears to be insensitive to the pretreatment, whereas the curve-fitting constant n_2 corresponding to the fast-fracture region III varies considerably.

Unlike with the bulk glass-like materials [53–57] where crack-tip plasticity does not occur, the detailed kinetics of environmentally assisted crack growth along polymer/metal interfaces is poorly understood because of the complexity at the crack tip. The current system includes a toughened epoxy, which involves nonlinear energy dissipation processes such as cavitation and shear yielding [58]. The macrorough substrates lead to the inhomogeneous interfacial stress distribution [2] and crack-surface contact [59]. In addition, crack-tip blunting may also take place because of the plasticity on the epoxy side for the strong interfaces; thus the situation becomes further complicated. Therefore, a theoretical prediction of the relation between crack velocity and energy-release rate seems to be too uncertain at this point. Nevertheless, the observed strong dependence of the energy-release rate on crack-growth velocity reveals that certain chemical reactions involving water at the crack tip must be responsible for the degradation of the epoxy/aluminum joints; presumably these reactions may be assisted by the stress acting at the crack tip.

3.3. Analysis of Locus of Failure

3.3.1. Crack-Tip Region

Visual inspection of the fracture surfaces on the aluminum side at the crack-tip region suggests that the failure is interfacial for all
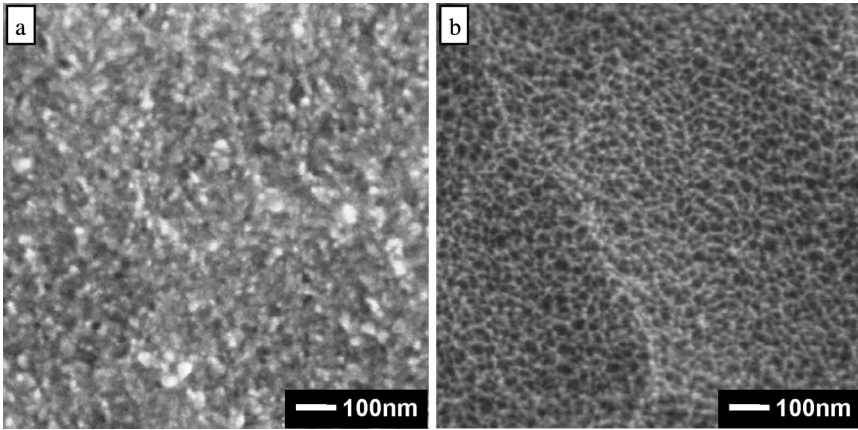
FIGURE 11 SEM photograph of the aluminum fracture surface at the crack-tip region for a joint with FPL-etched substrate (a) as compared to FPL-etched control surface before sol-gel application (b). The larger less distinct features in Figure 11a are due to a thin layer of sol-gel on the surface.

the pretreatments. SEM examinations revealed that a thin layer of sol-gel exists on the aluminum side for the FPL-etched substrate (Figure 11), whereas for the other pretreated substrates, SEM did not provide any more significant information than visual inspection because the aluminum fracture surfaces become rather featureless at high magnifications.

XPS analysis of the fracture surfaces reveals more about the failure mechanisms of sol-gel-treated epoxy/aluminum joints in humid environments (Figure 12). The distribution of the elements on the fracture surfaces at the crack-tip region is found to be independent of the pretreatment, although the amount of each element varies considerably with the type of surface pretreatment. Figure 13 is a schematic summarizing the elemental distribution on the fracture surfaces for all the pretreatments. In each case, the crack passes through the sol-gel layer because silicon and zirconium are detected on both the aluminum and epoxy sides regardless of the pretreatment. Considerable amounts of aluminum found on the epoxy side suggest that the crack partially passes through the oxide layer. In addition, anomalously high amounts of nitrogen are observed on the aluminum side, indicating that the curing agent is able to diffuse into the sol-gel layer.

By comparing the silicon and zirconium concentrations on the aluminum and epoxy sides at the crack-tip region for different pretreatments, it is evident that the locus of failure is weakly dependent

on the type of pretreatment (Figure 12). For the polished and sanded substrates, the amounts of silicon and zirconium found at the crack-tip region on the epoxy side are considerably higher than those on the aluminum side. Furthermore, the amounts of zirconium detected on the aluminum side are almost negligible compared with those detected on the sol-gel film before bonding, indicating that the cracks are very
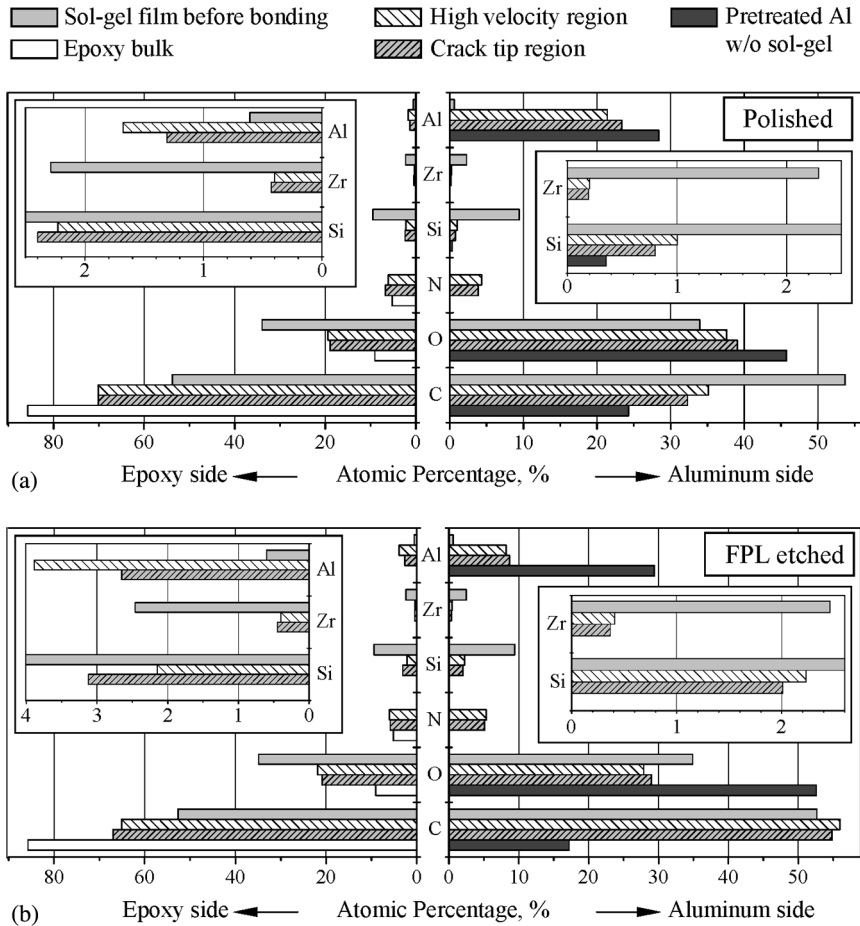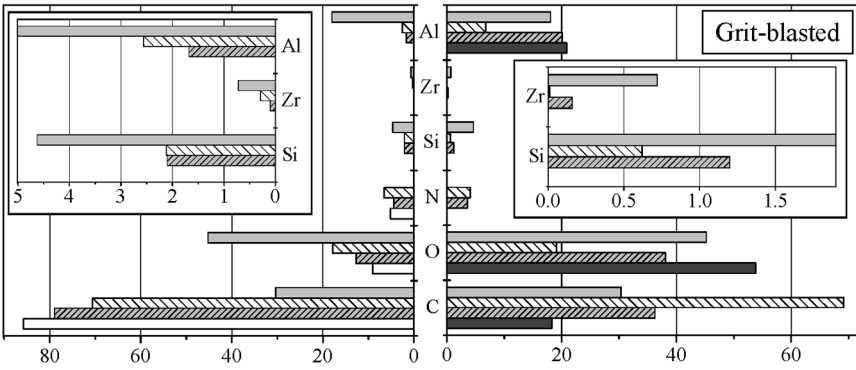

FIGURE 12 XPS atomic percentage data of fracture surfaces on aluminum and epoxy sides at the high-velocity and crack-tip regions for sol-gel-treated Al epoxy/joints prepared with various pretreatments compared to controls (sol-gel film before bonding, epoxy bulk and pretreated Al prior to sol-gel): (a) polished; (b) FPL etched; (c) sanded; (d) grit-blasted; (e) grit-blasted + FPL.
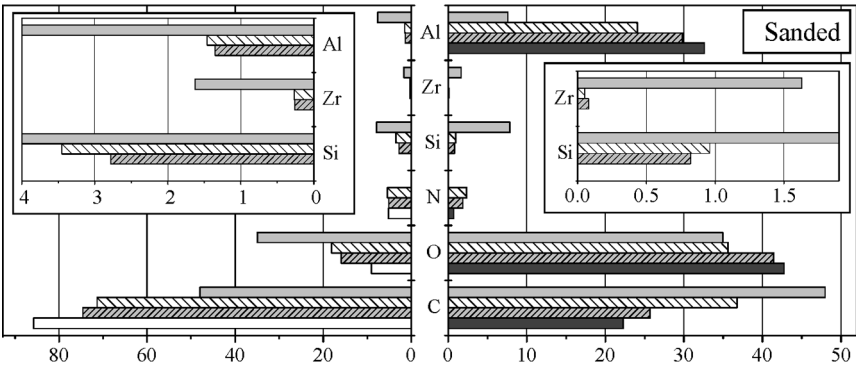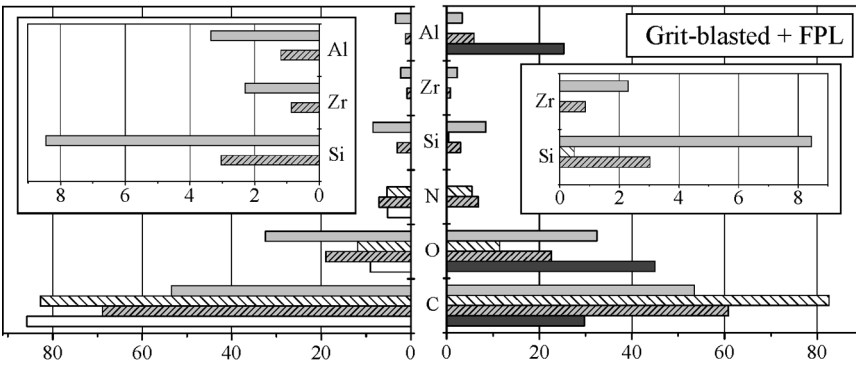
FIGURE 12 Continued.
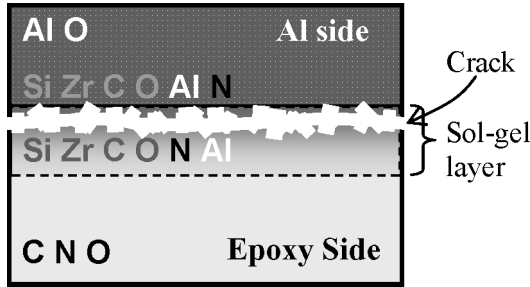
FIGURE 13 Schematic of the crack path at the crack tip region for the sol-gel-treated epoxy/aluminum joints.

close to the aluminum substrate. For the FPL-etched and grit-blasted substrates, the amounts of silicon and zirconium found at the crack-tip region of the epoxy side are comparable with those on the aluminum side, suggesting that the crack partially penetrates the sol-gel layer. For the "grit-blasted + FPL" substrate, the failure is certainly cohesive within the sol-gel, as indicated by the fact that the amounts of silicon and zirconium found at the aluminum and epoxy sides are almost identical; furthermore, the amounts of carbon and oxygen on the aluminum side and epoxy side are comparable with each other.

A detailed XPS regional scan on fracture surfaces provides information about how the sol-gel film interacts with the epoxy during the bonding process. Figure 14 compares the C1s spectra of the fracture surface at the crack-tip region on the aluminum and epoxy sides with the polished control substrate. Using the curve-fitting procedure, the ratios of the C−C/C−O and C−C/C−N are determined (Table 4). The C−C/C−O ratio for the aluminum side fracture surface is in between those of the aluminum control before sol-gel application and sol-gel film before bonding. This is consistent with the scenario that the crack passes through the sol-gel layer. The C−N species observed on the aluminum side undoubtedly come from the curing agent. The C−C/C−O and C−C/C−N ratios for the epoxy side fracture surface are in between those of the epoxy bulk and sol-gel film before bonding, indicating that the fracture surface on the epoxy side is partially epoxy and partially sol-gel in nature. The shake-up peak at about 291.8 eV, corresponding to the benzene group of the DGEBA monomer, is observed on the fracture surface on the epoxy side. This is an indication that the monomer of the epoxy resin is able to diffuse into the sol-gel layer. Presumably, the diffused monomer and curing agent are cross-linked with the sol-gel network.
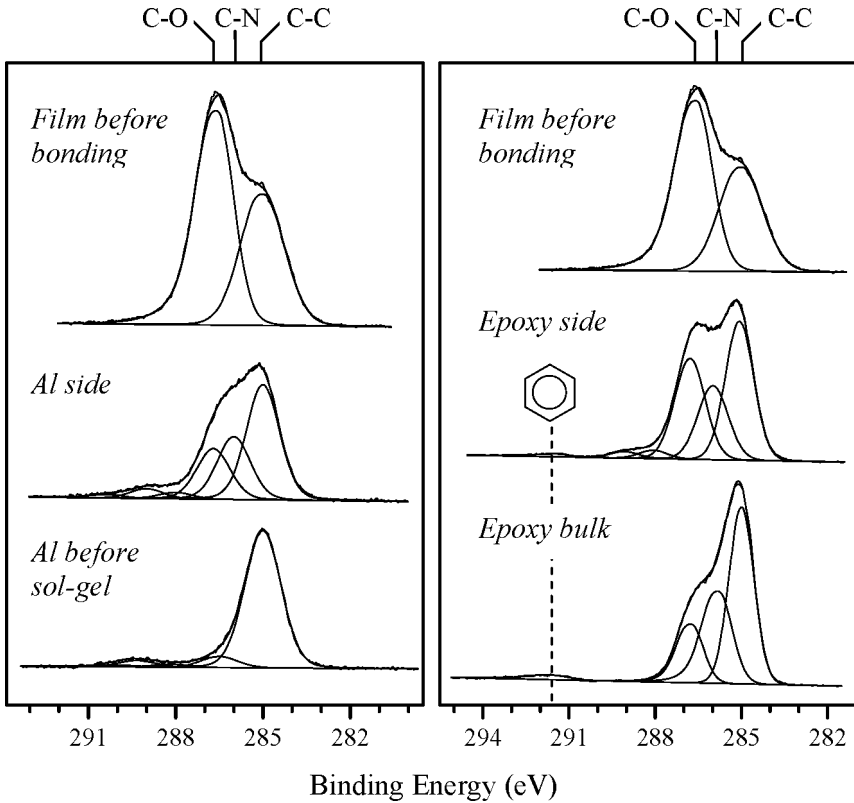
FIGURE 14 XPS C1s spectra of the fracture surface at the crack-tip region on the aluminum and epoxy sides compared to those of the control surfaces.

3.3.2. High-Velocity Region

On the fracture surfaces at the high-velocity region, stress whitening can be seen visually on the epoxy side for all the substrates except the polished one, indicating that an external toughening mechanism

TABLE 4 C−C/C−O and C−C/C−N Ratios Determined from the Curve Fitting in Figure 14 for Various Samples

Bond ratio	Al before sol-gel	Al side	Film before bonding	Epoxy side	Epoxy bulk (measured)	Epoxy bulk (theoretical[a])
C−C/C−O	11.95	2.02	0.67	1.33	2.70	2.61
C−C/C−N	N/A	2.28	N/A	1.81	1.51	1.44

[a]Calculated value based on epoxy formulation.

such as cavitation took place during the fracture process. The whitening fades away gradually in the direction of crack growth, in other words, as the energy-release rate decreases. Table 5 summarizes the results of visual inspection of the fracture surfaces at the high-velocity region and the corresponding energy-release rates for different pretreatments. It can be seen that there is a critical point with energy-release rate greater than $400 \, \mathrm{J/m^2}$, below which the stress whitening does not occur.

Visual inspection of the aluminum side at the high-velocity region suggested that fractured epoxy is left on several pretreated substrates. This observation was confirmed by SEM for the sanded, grit-blasted, and "grit-blasted + FPL" substrates (Figure 15). For these substrates, the elemental distribution on fracture surfaces at the high-velocity region is very similar to that at the crack-tip region (Figures 12, 13), indicating that cracks at the visually interfacial areas pass through the sol-gel layer. For polished and FPL-etched substrates, no epoxy is seen with SEM on the aluminum side in the high-velocity region. For these two substrates, the XPS elemental percentage data show little variance for the high-velocity and crack-tip regions (Figures 12a and 12b).

An intriguing observation regarding the locus of failure in the high-velocity region is that the amount of cohesive failure of epoxy changes significantly as the pretreatment changes, from 0% on polished and FPL-etched substrates to 100% on the "grit-blasted + FPL" substrate (Table 5, Figure 15). This indicates that there is a critical length scale for the size of the roughness features on the substrates below which the cohesive failure of epoxy does not occur. In other words, the macro-rough structures on the substrate are essential to drive the fracture to within the epoxy for the sol-gel-reinforced joints. It should be noted that the energy-release rate increases significantly as the amount of

TABLE 5 Energy-Release Rate and Visual Inspection Results of the Fracture Surfaces at the High-Velocity Region ($V = 7.6 \times 10^{-5} \, \mathrm{m/s}$) for Joints with Different Surface Preparation Methods

Surface pretreatment	$G \, \mathrm{J/m^2}$	Whitening on epoxy side	Locus of failure
Polished	435.6	No	Interfacial
FPL etched	1221.1	Yes	Interfacial
Sanded	1378.3	Yes	5% cohesive
Grit-blasted	2040.9	Yes	40% cohesive
Grit-blasted + FPL	2963.9	Yes	100% cohesive

*Note*: Data were obtained on one sample for each surface preparation.
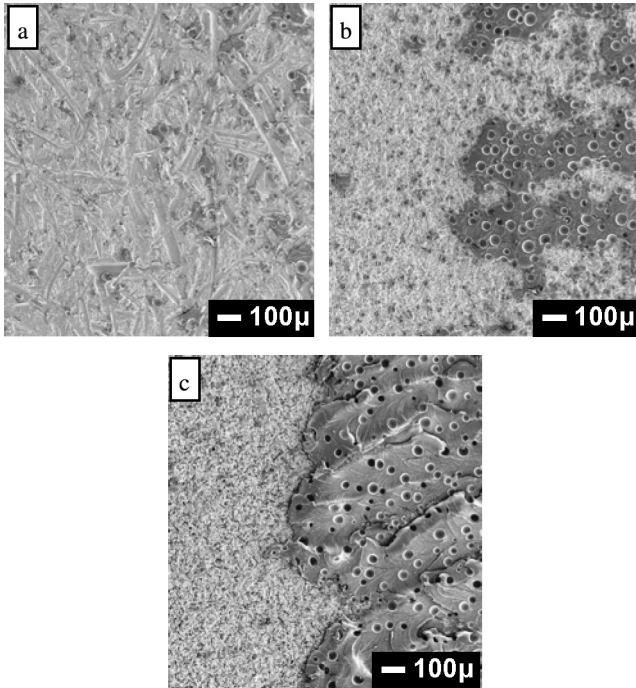
FIGURE 15 SEM photographs of the fracture surfaces on the aluminum side for joints with different pretreatments: (a) 120-grit sanded; (b) grit-blasted; (c) grit-blasted + FPL.

cohesive failure of epoxy increases (Table 5). This suggests that the energy dissipated at the crack tip is dominated by the bulk processes occurring on the epoxy side. Presumably, the onset of the cohesive failure within the epoxy is due to the changes in the local mode mixity [60] induced by the macrorough structures and thus enhances the initial strength.

3.4. Effect of Surface Morphology on Energy-Release Rate

To find out the correlation between surface morphology and energy-release rate, the critical energy-release rate, G_c, and threshold energy-release rate, G_{th}, are plotted as a function of average roughness, R_a, and fractal dimension, D, respectively (Figure 16). Because the accurate estimate of the fractal dimension for polished and FPL-etched substrates are not available, these two pretreatments are treated separately from the macrorough substrates (Figures 16b and
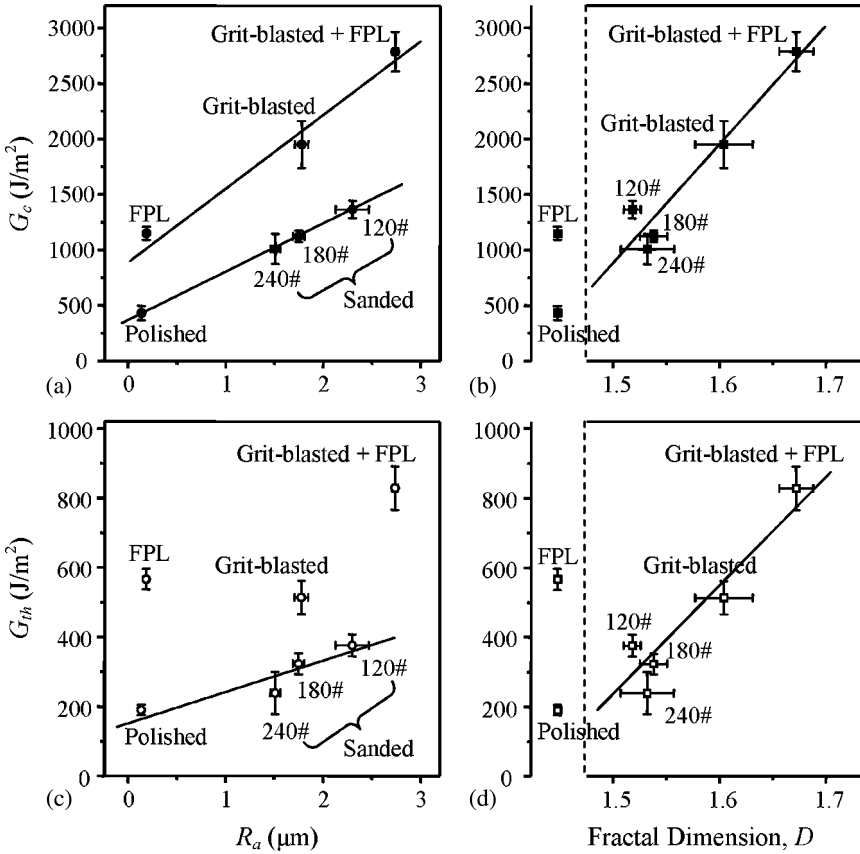
FIGURE 16 Critical fracture energy G_c, and threshold fracture energy, G_{th}, of the sol-gel-treated epoxy/aluminum joints *versus* average roughness, R_a, and fractal dimension, D: (a) G_c *vs.* R_a; (b) G_c *vs.* D; (c) G_{th} *vs.* R_a; (d) G_{th} *vs.* D. The G_c and G_{th} values are obtained from three measurements on different samples for each pretreatment; 120#, 180#, 240# represent the grit sizes of the sandpaper.

d). From the R_t data (Table 2), the dimensions of the micron-scale roughness features on the polished and FPL-etched substrates are approximately 1–2 µm. This value is far below the cohesive zone size estimated for the present system (10.5–62.5 µm) [61,62]. (The intrinsic fracture energy, G_0, was assumed to be 2–10 J/m² for the estimation, which seems to be reasonable for strongly covalently/ionically bonded interfaces as pointed out in Ref. [62]). Therefore, the polished and FPL-etched substrates are essentially smooth compared with the

macrorough substrates. For this reason, the G_c or G_{th} values for polished and FPL-etched substrates are plotted to the left of all the macrorough substrates in Figures 16b and 16d.

A good correlation (Figure 16a) can be found between the G_c and R_a for the substrates pretreated with abrasion techniques (polishing and sanding), showing that the G_c increases with R_a. A separate trend line can be drawn for the rest of the pretreatments. A correlation cannot be unified for all the pretreatments, possibly because of the differences of surface topography created by different pretreatments, which are not characterized by the traditional roughness parameters such as R_a. It must also be pointed out that although the surface chemistry varies with pretreatment, its role was not considered in the present study.

Although no unifying correlation between G_c and R_a has been found, a much better correlation is seen when G_c is plotted against the fractal dimension of all the macrorough substrates (Figure 16b). The existence of this correlation, however, is not easily understood, as the loci of failure at the high-velocity region are partially or totally within the bulk of epoxy. Nevertheless, the fact that the amount of cohesive failure within the epoxy depends on the macroroughness suggests that further studies should be directed toward understanding how the surface roughness affects the local stress field as well as the mode mixity.

As far as the threshold energy-release rate is concerned, although a limited correlation between G_{th} and R_a is observed for the abraded surfaces (Figure 16c), the correlation is not general for other surfaces. This lack of correlation is understandable because the G_{th} is significantly lower than the G_c and the locus of failure for the threshold region is closer to the aluminum substrates compared with the fast fracture region. On the other hand, the G_{th} correlates with the fractal dimension rather well (Figure 16d). This correlation is somewhat expected as the locus of failure at the threshold region follows the contour of the substrates; in other words, no cohesive failure within epoxy was observed, and the fracture surface on the aluminum side is visually identical to the substrate before bonding.

It is worth pointing out here that although the polished and FPL-etched substrates are both macroscopically flat, the energy-release rate on the FPL-etched substrate is significantly higher than that of the polished substrate. The G_c for FPL etched substrate is comparable with the macrorough sanded substrates, whereas its G_{th} value is even higher than that of the grit-blasted substrate. This is due to the interlocking effect induced by the nanoscale pores, which are only observed on the FPL-etched surfaces (Figure 7). The fracture surface on the aluminum side for FPL-etched substrates shows that part

of the sol-gel film is trapped in the pores, suggesting that the crack does not exactly follow the contour of the substrate (Figure 11). The energy-release rate is thus enhanced by pinning of the crack. The crack-pinning effect has been demonstrated by Chung and Chaudhury [63] on a thin confined adhesive pad with designed discontinuity. Interestingly, a similar effect becomes more pronounced as the crack velocity decreases, indicating that the nanoscale structures on the substrate are more important than the macroroughness in enhancing the durability of the joints.

4. CONCLUSIONS

Using an ADCB wedge test, the moisture-assisted crack-growth kinetics of a sol-gel-reinforced epoxy/aluminum interface was studied. The fracture mechanics approach provides an effective way of studying the effect of surface pretreatment on adhesion. It is found that the surface morphology and topography affect the crack-growth kinetics significantly. The macrorough structures were found to be essential to drive the crack to within the epoxy and thus enhance the initial strength of the sol-gel-reinforced interface. However, the microroughness of the substrate is more important than the macroroughness in enhancing the durability. Lastly, both the critical energy-release rate and threshold energy-release rate correlate with the fractal dimension for sol-gel-reinforced joints with macrorough substrates.

ACKNOWLEDGMENTS

REFERENCES

[1] Kinloch, A. J., in *Adhesion Science and Engineering 1, The Mechanics of Adhesion*, D. A. Dillard and A. V. Pocius (Eds.) (Elsevier Science, Amsterdam, The Netherlands, 2002), pp. 661–698.
[2] Kinloch, A. J., *Adhesion and Adhesives: Science and Technology* (Chapman and Hall, London, UK, 1987).
[3] Kinloch, A. J., in *Polymer Surfaces and Interfaces*, W. J. Feast and H. S. Munro (Eds.) (John Wiley & Sons, Ltd., New York, 1987), pp. 75–97.

[4] Davis, G. D. and Venables, J. D., in *Adhesion Science and Engineering 2, Surface, Chemistry and Applications*, M. K. Chaudhury and A. V. Pocius (Eds.) (Elsevier Science, Amsterdam, The Netherlands, 2002), pp. 947–1008.

[5] Plueddemann, E. P., *Silane Coupling Agents* 2nd ed. (Plenum Press, New York, 1991).

[6] Mittal, K. L. Ed., *Silane and Other Coupling Agents*, (VSP, Leiden, The Netherlands, 1992), Vol. 1.

[7] Mittal, K. L., Ed., *Silane and Other Coupling Agents*, (VSP, Leiden, The Netherlands, 2000), Vol. 2.

[8] Mittal, K. L., Ed., *Silane and Other Coupling Agents*, (VSP, Leiden, The Netherlands, 2004), Vol. 3.

[9] Owen, M. J., in *Adhesion Science and Engineering 2, Surface, Chemistry and Applications*, M. K. Chaudhury and A. V. Pocius (Eds.) (Elsevier Science, Amsterdam, The Netherlands, 2002), pp. 403–431.

[10] Abel, M.-L., Watts, J. F., and Digby, R. P., *J. Adhes.* **80**, 291–312 (2004).

[11] Blohowiak, K. Y., Osborne, J. H., and Krienke, K. A., US Patents 05 814 137 (1998), 05 849 110 (1998), 5 869 140 (1999), 5 869 141 (1999), 5 939 197 (1999), and 6 037 060 (2000).

[12] Osborne, J. H., Blohowiak, K. Y., Taylor, S. R., Hunter, C., Bierwagon, G., Carlson, B., Bernard, D., and Donley, M. S., *Prog. Org. Coatings* **41**, 217–225 (2001).

[13] Blohowiak, K. Y., Krienke, K. A., Osborne, J. H., Mazza, J. J., Gaskin, G. B., Arnold, J. R., DePiero, W. S., and Brescia, J., *The Second Joint NASA/FAA/DoD Conference on Aging Aircraft* (Williamsburg, VA, 1998), pp. 313–320.

[14] Blohowiak, K. Y., Osborne, J. H., Krienke K. A., and Sekits, D. F., *28th International SAMPE Symposium* (Seattle, WA, 1996), pp. 440–446.

[15] Blohowiak, K. Y., Cadwell-Stancin, L., Anderson, R. A., Mazzitelli, C. M., Preedy, K., Grob, J. W., and Glidden, M., 47th *International SAMPE Symposium* (Long Beach, CA, 2002), pp. 279–292.

[16] Greegor, R. B., Blohowiak, K. Y., Osborne, J. H., Krienke, K. A., and Cherian, J. T., *J. Sol-gel Sci. Technol.* **20**, 35–50 (2001).

[17] McCray, D. B. and Mazza, J. J., *45th International SAMPE Symposium* (Long Beach, CA, 2000), pp. 42–56.

[18] Huber, K. E., McCray, D. B., and Srinivasan, R., *Proc. Processing and Fabrication of Advanced Materials IX* (St. Louis, MO, 2001), pp. 53–62.

[19] Brown, H. R., *Macromolecules* **22**, 2859–2860 (1989).

[20] Creton, C., Kramer, E. J., Hui, C.-Y., and Brown, H. R., *Macromolecules* **25**, 3075–3088 (1992).

[21] Xiao, F., Hui, C.-Y., Washiyama, J., and Kramer, E. J., *Macromolecules* **27**, 4382–4390 (1994).

[22] Bernard, B., Brown, H. R., Hawker, C. J., Kellock, A. J., and Russell, T. P., *Macromolecules* **32**, 6254–6260 (1999).

[23] Creton, C., Kramer, E. J., Brown, H. R., and Hui, C.-Y., *Advances in Polymer Science* **156**, 53–136 (2001).

[24] Liu, J., Chaudhury, M. K., Berry, D. H., Seebergh, J. E., Osborne, J. H., and Blohowiak, K. Y., *J. Adhes. Sci. Technol.*, **20**, 277–305 (2006).

[25] Bagheri, R. and Pearson, R. A., *Polymer* **37**, 4529–4538 (1996).

[26] Bagheri, R. and Pearson, R. A., *Polymer* **41**, 269–276 (2000).

[27] Venables, J. D., *J. Mater. Sci.* **19**, 2433–2453 (1984).

[28] Kanninen, M. F., *Int. J. Fracture* **9**, 83–92 (1973).

[29] Xiao, F., Hui, C.-Y., and Kramer, E. J., *J. Mater. Sci.* **28**, 5620–5629 (1993).

[30] Zhang, S., Panat, R., and Hsia, K. J., *J. Adhes. Sci. Technol.* **17**, 1685–1711 (2003).

[31] *Mountains Map* Software Manual, Micro Photonics Inc., Irvine, CA (2005).

[32] ISO 4287, *Geometrical Product Specifications (GPS)—Surface Texture: Profile Method—Terms, Definitions and Surface Texture Parameters*, International Organization for Standardization, Geneva, Switzerland (1997).

[33] Mandelbrot, B. B., *The Fractal Geometry of Nature* (Freeman, San Francisco, CA, 1982).

[34] Russ, J. C., *Fractal Surfaces* (Plenum Press, New York, 1994), pp. 227–265.

[35] Sapoval, B., in *Fractals and Disordered Systems*, A. Bunde and S. Havlin (Eds.) (Springer-Verlag, Berlin, Germany, 1991), pp. 207–227.

[36] Amada, S. and Yamada, H., *Surf. Coat. Technol.* **78**, 50–55 (1996).

[37] Amada, S. and Hirose, T., *Surf. Coat. Technol.* **102**, 132–137 (1998).

[38] Amada, S. and Satoh, A., *J. Adhes. Sci. Technol.* **14**, 27–41 (2000).

[39] Mannelqvist, A. and Groth, M. R., *Appl. Phys. A* **73**, 347–355 (2001).

[40] Lopez, J., Miller, C. A., and Ruckenstein, E., *J. Colloid Interface Sci.* **56**, 460–468 (1976).

[41] Bascom, W. D. and Singleterry, C. R., *J. Colloid Interface Sci.* **66**, 559–572 (1978).

[42] Tanner, L. H., *J. Phys. D* **12**, 1473–1484 (1979).

[43] Marmur, A., *Adv. Colloids Interface Sci.* **19**, 75–102 (1983).

[44] de Gennes, P. G., *Rev. Modern Phys.* **57**, 827–863 (1985).

[45] Cazabat, A. M. and Cohen Stuart, M. A., *J. Phys. Chem.* **90**, 5845–5849 (1986).

[46] Lin, C. M., Ybarra, R. M., and Neogi, R., *Adv. Colloids Interface Sci.* **67**, 185–204 (1996).

[47] Marmur, A., *Colloids and Surfaces A: Physicochem. Eng. Aspects* **250**, 409–414 (2004).

[48] Chaudhury, M. K. and Chaudhury, A., *Soft matter* **1**, 431–435 (2005).

[49] Krausz, A. S. and Krausz, K., *Fracture Kinetics of Crack Growth* (Kluwer Academic Publishers, Dordrecht, The Netherlands, 1988).

[50] Martin, R. H. and Murri, G. B., in *Composite Materials: Testing and Design*, S. P. Garbo (Ed.) (ASTM, STP 1059, 1990), Vol. 9 pp. 251–270.

[51] Kinloch, A. J. and Osiyemi, S. O., *J. Adhes.* **43**, 79–90 (1993).

[52] Ritter, J. E., Fox, J. R., Hutko, D. I., and Lardner, T. J., *J. Mater. Sci.* **33**, 4581–4588 (1998).

[53] Wiederhorn, S. M., *J. Am. Ceram. Soc.* **50**, 407–414 (1967).

[54] Wiederhorn, S. M. and Bolz, L. H., *J. Am. Ceram. Soc.* **53**, 543–548 (1970).

[55] Lawn, B. R., *J. Mater. Sci.* **10**, 469–480 (1975).

[56] Wiederhorn, S. M., Freiman, S. W., Fuller, E. R., and Simmons, C. J., *J. Mater. Sci.* **17**, 3460–3478 (1982).

[57] Michalske, T. A. and Bunker, B. C., *J. Am. Ceram. Soc.* **76**, 2613–2618 (1993).

[58] Kinloch, A. J. and Young R. J., *Fracture Behaviour of Polymers* (Elsevier Science, New York, 1983).

[59] Evans, A. G. and Hutchinson, J. W., *Acta Metall.* **37**, 909–916 (1989).

[60] Hutchinson, J. W. and Suo, Z., *Adv. Appl. Mech.* **29**, 63–191 (1991).

[61] Tvergaard, V. and Hutchinson, J. W., *J. Mech. Phys. Solids* **41**, 1119–1135 (1993).

[62] Kook, S.-Y. and Dauskardt, R. H., *J. Appl. Phys.* **91**, 1293–1303 (2002).

[63] Chung, J. Y. and Chaudhury, M. K., *Journal of the Royal Society Interface* **2**, 55–61 (2005).